Nano Research Energy

ISSN 2791-0091 (print); 2790-8119 (online)
https://doi.org/10.26599/NRE.2026.9120227

Research Article

Taming the polyiodide shuttle *via* curvature engineering of cationic microenvironments for ultradurable Zn-I_2 batteries

Lin Zhou[1], Geyang Zhang[1], Wenyan Zan[1] (✉), Yunzhen Chang[1], Wenjing Hou[1], Yanping Li[1], Na Wang[2], Sheng Zhu[1,3] (✉), and Gaoyi Han[1,3] (✉)

[1] *Institute of Molecular Science, Key Laboratory of Energy Storage Materials Innovation and Integration Shanxi Province, Key Laboratory of Chemical Biology and Molecular Engineering of Education Ministry, Shanxi University, Taiyuan 030006, China*
[2] *Department of Materials Science and Engineering, Jinzhong University, Jinzhong 030619, China*
[3] *Institute for Carbon-Based Thin Film Electronics, Peking University-Shanxi (ICTFE-PKU), Taiyuan 030012, China*

Received: 30 January 2026 / **Revised:** 18 March 2026 / **Accepted:** 25 March 2026 / **Published date:** 17 April 2026

ABSTRACT

Aqueous zinc-iodine batteries (AZIBs) are promising candidates for grid-scale energy storage owing to their high safety and low cost. However, their practical application is hindered by severe polyiodide species shuttle. Herein, we have constructed well-defined cationic microenvironments by assembling poly(diallyldimethylammonium chloride) (PDDA) onto multi-walled carbon nanotubes (PDDA@MWCNT) and flat graphite sheets (PDDA@GS). This design enables strong electrostatic anchoring of polyiodide species and allows systematic differentiation of curvature-dependent immobilization behaviors. The optimal PDDA@MWCNT cathode exhibits a high Coulombic efficiency of 98.3% at 0.1 $A \cdot g^{-1}$, along with exceptional durability of 82,000 cycles at 3.0 $A \cdot g^{-1}$ and 3,569 cycles at 0.1 $A \cdot g^{-1}$ (nearly one year), far surpassing its planar PDDA@GS counterpart. Combined experimental characterizations and density functional theory (DFT) calculations reveal that the curvature-guided PDDA configuration markedly enhances iodine adsorption and accelerates interfacial charge transfer, thereby suppressing polyiodide shuttling and self-discharge. This work demonstrates molecular curvature engineering as a powerful and generalizable strategy for governing iodine chemistry, offering new design principles for high-performance AZIBs.

KEYWORDS

Zn-I_2 battery, polyiodide shuttle, cationic microenvironments, confinement, curvature engineering

1 Introduction

The rapid global transition toward renewable energy has accelerated the demand for large-scale and sustainable energy storage systems to maintain grid stability [1–3]. Among the various candidates, rechargeable aqueous zinc-iodine batteries (AZIBs) have attracted increasing attention due to their high theoretical capacity (211 $mAh \cdot g^{-1}$ for iodine), intrinsic safety derived from aqueous electrolytes, and cost-effectiveness based on earth-abundant zinc [4, 5]. However, the practical implementation of AZIBs is severely hindered by the notorious polyiodide shuttle effect and sluggish redox conversion kinetics, leading to low Coulombic efficiency, rapid capacity fading, and poor rate performance [6–8]. These issues primarily originate from the thermodynamically favored association between molecular iodine and iodide ions, which generates water-soluble triiodide intermediates (I_3^-) that readily diffuse to the zinc anode, triggering undesired redox reactions to damage the performance of the battery [9–11].

To mitigate the shuttle effect, various strategies have been developed, including cathode host optimization [12, 13], ion-selective membrane modification [14, 15], electrolyte regulation [16, 17], and anode protection [18, 19]. Among them, the rational design of cathode host materials has proven to be one of the most common approaches for immobilizing soluble polyiodide species. Notably, carbon-based materials owing to their high surface area, excellent conductivity, and structural stability have been considered as ideal hosts [20–22]. Nevertheless, their intrinsically electroneutral or negatively charged surfaces exhibit weak interactions with polyiodide ions, providing limited immobilization capability [23, 24]. Therefore, constructing interfacial architectures that enable strong host-guest electrostatic interactions remains a central challenge for suppressing polyiodide migration. Recent advances in electrochemical systems have revealed that nanoscale geometry and local curvature can profoundly influence ion transport, charge redistribution, and interfacial reactions [25–28]. In particular, curvature-engineered carbon nanostructures have been

© The Author(s) 2026. Published by Tsinghua University Press. The articles published in this open access journal are distributed under the terms of the Creative Commons Attribution 4.0 International License (http://creativecommons.org/licenses/by/4.0/), which permits use, distribution and reproduction in any medium, provided the original work is properly cited.

Address correspondence to Gaoyi Han, han_gaoyis@sxu.edu.cn; Sheng Zhu, shengzhu@sxu.edu.cn; Wenyan Zan, zanwy@sxu.edu.cn

demonstrated to tailor local electronic states and optimize catalytic activity by modulating charge density and adsorption sites, emphasizing the pivotal role of geometric environments in governing interfacial functionality [29–32].

Based on above-mentioned insights, integrating structural curvature engineering with electrostatic interfacial design may offer a promising strategy to regulate redox processes at the electrode-electrolyte interface in energy storage systems. Within AZIBs, the cationic polymer poly(diallyldimethyl ammonium chloride) (PDDA) has demonstrated unique advantages in immobilizing anionic redox intermediates *via* strong electrostatic confinement [33–36]. Nevertheless, how the molecular conformation of PDDA and the spatial arrangement of its quaternary ammonium sites collectively govern iodine adsorption and redox reversibility remains insufficiently understood. Such molecular-level insights are crucial for rationally suppressing the shuttle effect and achieving highly reversible iodine electrochemistry in AZIBs. To probe these molecular-level insights, we have constructed cationic microenvironments with well-defined curvatures by noncovalently assembling PDDA onto multi-walled carbon nanotubes (MWCNT) with different diameters, complemented by planar graphite sheets (GS) as a flat reference. The coaxial tubular geometry of MWCNT induces a conformally curved PDDA layer, whereas GS provides a planar interface for comparison. This platform with tunable curvature enables a systematic evaluation of the influence of nanoscale geometry on iodine adsorption strength and redox reaction kinetics. Combined experimental and theoretical analyses reveal that the carbon substrate curvature optimizes the PDDA interface, thereby generating a cooperative effect between electrostatic confinement and reaction kinetics. Such curvature-mediated synergy effectively suppresses polyiodide shuttling and enhances redox reversibility. Overall, this work establishes a framework for "molecular curvature engineering" in AZIBs, highlighting the decisive role of interfacial microenvironments and providing a generalizable design principle for high-performance redox-based energy storage systems.

2 Results and discussion

To construct curvature regulated carbon hosts for Zn-I_2 batteries, PDDA was conformally coated onto carbon substrates with distinct geometries, including planar graphite (GS) and multiwalled carbon nanotubes (MWCNT) with different diameters. The geometric curvature (κ) of the carbon substrates is defined as $\kappa = 1/R$, where R represents the radius of the nanotube. According to their diameters, the MWCNT samples were categorized as MWCNT-H, MWCNT-M, and MWCNT-L, corresponding to high, medium, and low surface curvature, respectively. As schematically illustrated in Figs. 1(a) and 1(b), the negatively charged oxygen-containing functional groups on MWCNT surfaces enable spontaneous electrostatic assembly of

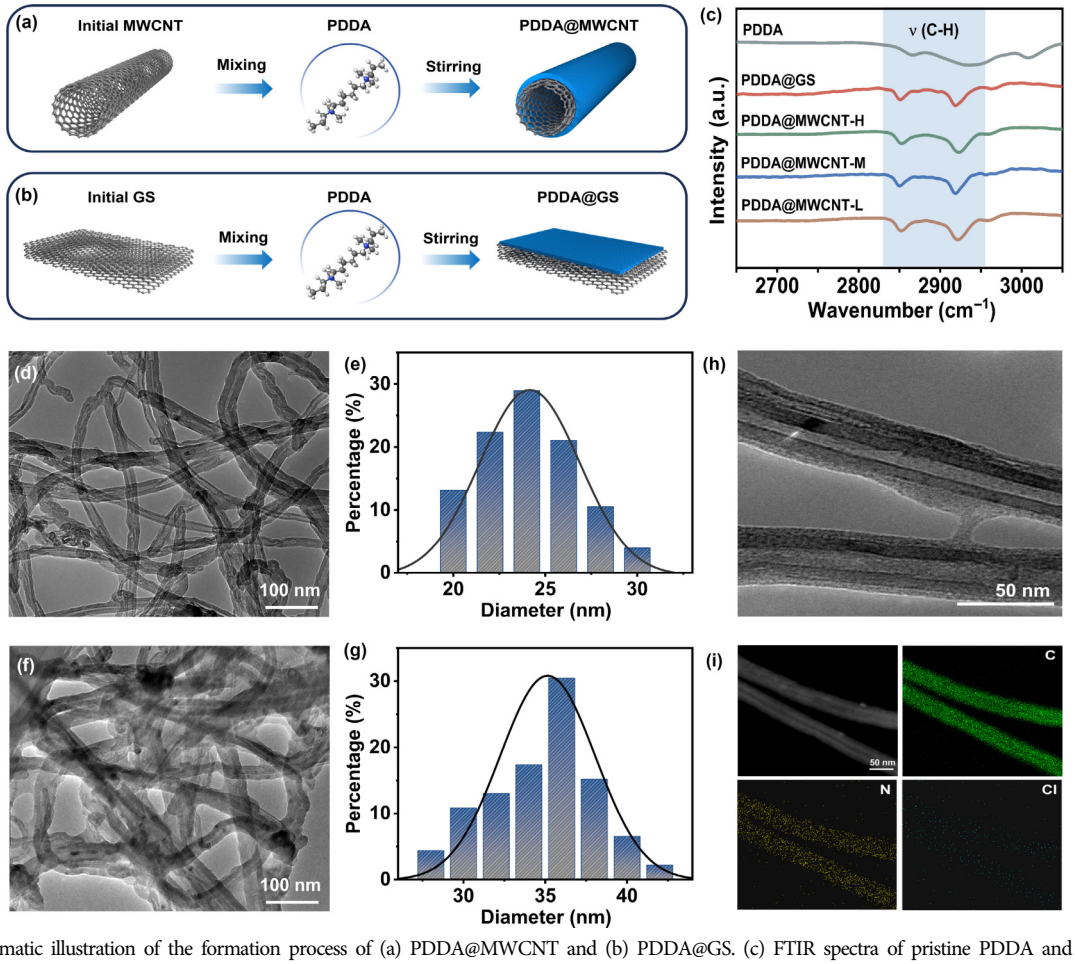

Figure 1 Schematic illustration of the formation process of (a) PDDA@MWCNT and (b) PDDA@GS. (c) FTIR spectra of pristine PDDA and PDDA-coated substrates. (d) TEM image of the pristine MWCNT-M. (e) Statistical diameter distribution of the pristine MWCNT-M derived from TEM analysis. (f) TEM image of the PDDA@MWCNT-M. (g) Statistical diameter distribution of the PDDA@MWCNT-M derived from TEM analysis. (h) High-magnification TEM image of PDDA@MWCNT-M. (i) Corresponding elemental mapping of PDDA@MWCNT-M.

positively charged PDDA chains at room temperature, forming a conformal polymer layer along the outer walls. In comparison, PDDA adsorption on planar GS form a thin, flat polymer film via similar electrostatic interactions. The successful coating of PDDA on these carbon substrates has been confirmed by Fourier-transform infrared (FTIR) spectroscopy (Fig. 1(c)), where the C–H symmetric (≈2876 cm^{-1}) and asymmetric (≈2915 cm^{-1}) stretching vibrations of PDDA gradually shift toward lower wavenumbers after interaction with MWCNT and GS, suggesting a weakened C–H bonding strength resulting from electronic coupling between PDDA and the carbon frameworks [37, 38].

Morphological characterizations further elucidate the surface features of these composites. Scanning electron microscopy (SEM) images reveal that pristine GS exhibits a smooth and layered morphology, which remains largely intact but with slightly roughened surfaces after PDDA modification (Fig. S1 in the Electronic Supplementary Material (ESM)), consistent with a thin polymer overlayer on the zero-curvature structure. For the curved models, MWCNT with outer diameters of 16 ± 4 nm (MWCNT-H), 24 ± 6 nm (MWCNT-M), and 38 ± 12 nm (MWCNT-L) exhibit uniform tubular architectures, as evidenced by transmission electron microscopy (TEM) images and statistical diameter distributions (Figs. 1(d) and 1(e) and Figs. S2 and S3 in the ESM). After PDDA modification, the nanotubes retain structural integrity while gaining a continuous polymer coating, resulting in increased diameters of 28 ± 8 nm (PDDA@MWCNT-H), 36 ± 8 nm (PDDA@MWCNT-M), and 50 ± 12 nm (PDDA@MWCNT-L) (Figs. 1(f) and 1(g), and Figs. S4 and S5 in the ESM), which corresponds to a statistically averaged PDDA layer thickness of approximately 5–7 nm across different curvatures. This result demonstrates that electrostatic self-assembly effectively yields a conformal PDDA layer that matches the substrate geometry. High-resolution TEM and elemental mapping (Figs. 1(h) and 1(i)) further confirmed the uniform PDDA coating on MWCNT-M, providing a clearly defined curvature-regulated composite structure for subsequent electrochemical evaluation.

To evaluate the adsorption capacity of iodine species on PDDA-wrapped carbon materials, equal masses of the samples have been immersed in polyiodide solutions with the same volume and concentration. After standing for 3 hours, the color of the supernatant exhibited distinct differences (Fig. S6 in the ESM). The solution interacted with PDDA@MWCNT-M became nearly colorless, suggesting the most efficient adsorption of polyiodide species. Ultraviolet-visible (UV-Vis) spectroscopy (Fig. 2(a)) further quantitatively confirmed this observation, revealing that PDDA@MWCNT-M exhibits the most pronounced suppression of the I_3^- absorption band, indicating its strongest affinity for polyiodide species [35, 39, 40]. To isolate the contribution of the carbon substrate, control experiments have been conducted using GS and MWCNTs with varying curvatures. UV-vis spectra show that all substrates exhibit only weak I_3^- adsorption (Fig. S7 in the ESM), indicating that carbon curvature alone does not enable significant polyiodide immobilization. To assess the role of specific surface area (SSA) in adsorption, nitrogen sorption measurements have been measured (Fig. S8 in the ESM). GS exhibits the lowest

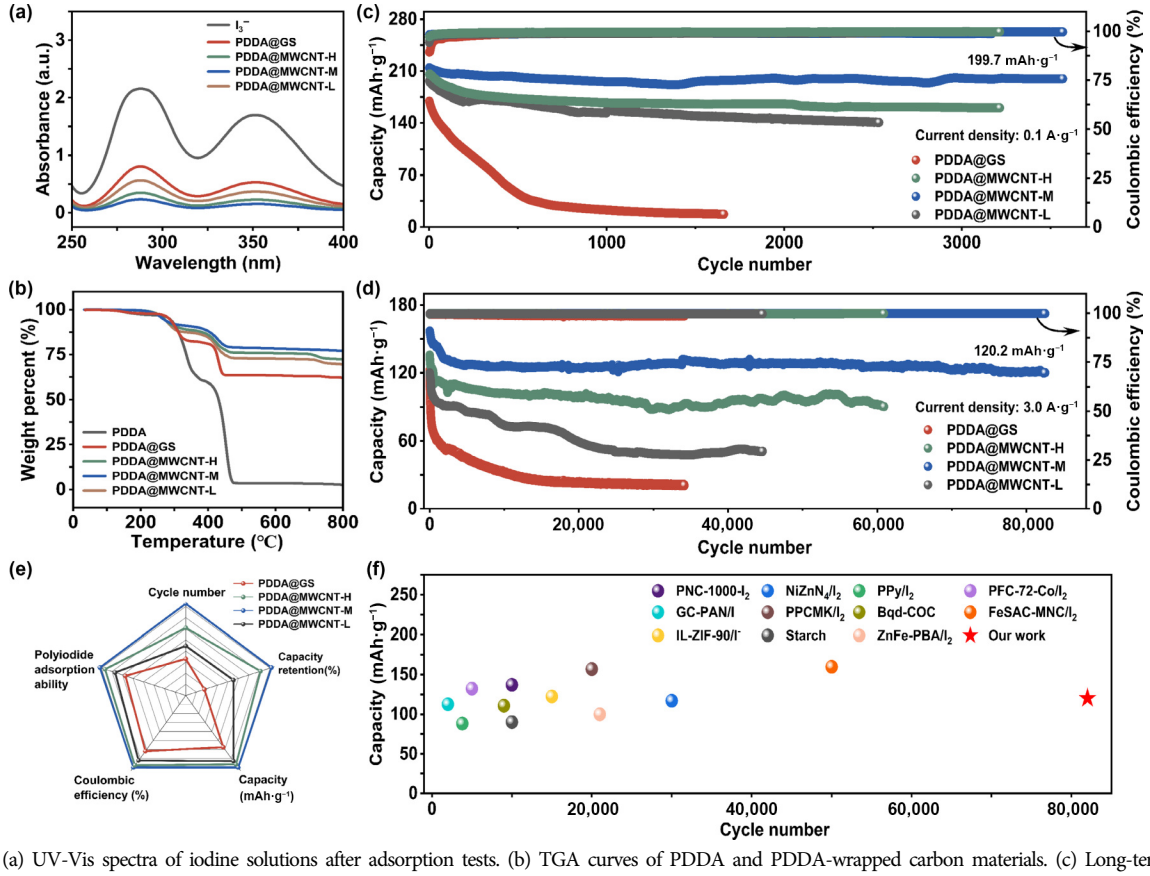

Figure 2 (a) UV-Vis spectra of iodine solutions after adsorption tests. (b) TGA curves of PDDA and PDDA-wrapped carbon materials. (c) Long-term cycling performance at 0.1 $A·g^{-1}$ at room temperature. (d) Long-term cycling performance at 3.0 $A·g^{-1}$ at room temperature for batteries of Zn||PDDA@MWCNT-H, Zn||PDDA@MWCNT-M, Zn||PDDA@MWCNT-L and Zn||PDDA@GS. (e) Radar plot summarizing cycle number, capacity retention, capacity, Coulombic efficiency, and polyiodide adsorption ability of Zn||PDDA@MWCNT-H, Zn||PDDA@MWCNT-M, Zn||PDDA@MWCNT-L, and Zn||PDDA@GS cells. (f) Comparison of this work with previously reported AZIBs in terms of reversible capacity and cycle life.

SSA (8.9 $m^2 \cdot g^{-1}$), while MWCNT samples show slight differences in SSA depending on their curvature: MWCNT-H (112.5 $m^2 \cdot g^{-1}$) > MWCNT-M (101.5 $m^2 \cdot g^{-1}$) > MWCNT-L (95.5 $m^2 \cdot g^{-1}$). However, the absence of correlation between SSA and adsorption capacity suggests that SSA is not the primary determinant for I_3^- binding. Given PDDA's electrostatic interaction with I_3^-, thermogravimetric analysis (TGA) quantified PDDA content (Fig. 2(b) and Fig. S9 in the ESM): PDDA@GS (37.2%) > PDDA@MWCNT-H (29.1%) > PDDA@MWCNT-L (26.7%) > PDDA@MWCNT-M (22.2%). Notably, there is no direct correlation emerged between PDDA content and iodine adsorption. The sample of PDDA@MWCNT-M exhibits the highest adsorption capacity despite the lowest PDDA loading. These findings imply that unaccounted microstructural factors govern adsorption behavior. To further evaluate the availability of surface cationic quaternary ammonium sites, zeta potential measurements have been conducted (Fig. S10 in the ESM). All PDDA-modified samples display strongly positive zeta potentials, confirming the successful exposure of cationic groups on the surfaces. Notably, PDDA@MWCNT-M exhibits the highest value (48.61 mV), followed by PDDA@MWCNT-H (44.23 mV), PDDA@MWCNT-L (40.04 mV), and PDDA@GS (38.78 mV). This result suggests that the surface electrostatic environment is not simply determined by the total PDDA quantity, but rather by the spatial configuration of PDDA chains on substrates with different curvatures. To quantitatively evaluate the curvature-dependent adsorption strength, adsorption isotherm experiments have been further conducted and the equilibrium data are fitted using the Langmuir adsorption model (Fig. S11 in the ESM). The fitting results indicate that the adsorption behavior of polyiodide species on PDDA-modified substrates follows a typical monolayer adsorption mechanism. Based on the Langmuir equilibrium constants, the corresponding Gibbs free energy changes (ΔG) for polyiodide adsorption are calculated according to $\Delta G = -RT\ln K$. The calculated ΔG values follow the order: PDDA@MWCNT-M (−24.24 kJ·mol^{-1}) < PDDA@MWCNT-H (−23.77 kJ·mol^{-1}) < PDDA@MWCNT-L (−22.81 kJ·mol^{-1}) < PDDA@GS (−22.42 kJ·mol^{-1}), indicating that the moderately curved PDDA@MWCNT-M provides the most thermodynamically favorable binding toward polyiodide species. These results quantitatively confirm that moderate curvature optimizes PDDA chain conformation and strengthens electrostatic interactions with polyiodides, thereby enhancing adsorption affinity. Integrating composition and performance data, MWCNT-based composites outperformed GS, with adsorption capacities following PDDA@MWCNT-M > PDDA@MWCNT-H > PDDA@MWCNT-L. This trend suggests a pivotal role for geometric curvature in polyiodide fixation. Insufficient curvature (MWCNT-L or planar GS) limits quaternary ammonium site exposure and electrostatic interactions, whereas excessive curvature (MWCNT-H) induces PDDA chain distortion and structural deformation, weakening binding. In contrast, moderate curvature (MWCNT-M) promotes an optimal PDDA conformation, maximizing quaternary ammonium accessibility and electrostatic affinity for polyiodides. Thus, the curvature-regulated PDDA molecular conformation is a key driver of adsorption performance.

To investigate whether the curvature-dependent adsorption strength translates into electrochemical advantages, Zn||PDDA@carbon materials cells have been systematically evaluated. At a current density of 0.1 $A \cdot g^{-1}$ (Fig. S12 in the ESM), the Zn||PDDA@MWCNT-M exhibits the highest discharge capacity and nearly 100% Coulombic efficiency (CE), significantly outperforming Zn||PDDA@MWCNT-H, Zn||PDDA@MWCNT-L, and Zn||PDDA@GS. For comparison, cathodes assembled with carbon materials (without PDDA modification) are also tested under identical conditions (Fig. S13 in the ESM). These cells show low Coulombic efficiencies (GS: 43.9%, MWCNT-L: 47.8%, MWCNT-M: 49.4%, and MWCNT-H: 48.4%), indicating limited intrinsic confinement of polyiodide species. In contrast, PDDA-coated counterparts exhibit significantly enhanced adsorption and electrochemical performance, confirming that the dominant suppression of the polyiodide shuttle arises from the synergistic coupling between the cationic PDDA layer and the curvature-optimized carbon substrate. Long-term cycling stability at 0.1 $A \cdot g^{-1}$ further confirms the exceptional durability of Zn||PDDA@MWCNT-M, retaining a high reversible capacity of 199.7 mAh·g^{-1} after 3569 cycles (over one year) with 93.7% capacity retention and nearly 100% CE (Fig. 2(c)). In comparison, the Zn||PDDA@MWCNT-H and Zn||PDDA@MWCNT-L suffer gradual capacity decay (with the trend in decay rate following Zn||PDDA@MWCNT-H < Zn||PDDA@MWCNT-L < Zn||PDDA@GS). The poor stability of Zn||PDDA@GS may originate from its planar geometry and absence of curvature, which leads to irreversible interlayer expansion during polyiodide intercalation, as confirmed by the shift of the X-ray diffraction (XRD) (002) diffraction peak from 27.19° (0.327 nm) to 26.95° (0.331 nm) after 100 cycles at 0.1 $A \cdot g^{-1}$ (Fig. S14 in the ESM). Meanwhile, the noticeable decrease in peak intensity indicates reduced stacking order and partial loss of interlayer coherence, suggesting that the structural expansion/shrinkage is not fully reversible [41, 42]. The rate performance further highlights the Zn||PDDA@MWCNT-M's kinetic advantages (Fig. S15 in the ESM), it delivers reversible capacities of 217.6, 202.5, 191.7, 174.3, and 157.6 mAh·g^{-1} at current densities of 0.1, 0.3, 0.5, 1.0, and 3.0 $A \cdot g^{-1}$, respectively. When the current density has been returned to 0.1 $A \cdot g^{-1}$, the capacity rapidly recovered to 217.2 mAh·g^{-1}, demonstrating excellent reversibility and fast charge-transfer kinetics. Based on the galvanostatic charge-discharge profiles, the gravimetric energy density of the assembled Zn-I_2 cells is further evaluated according to the mass of active materials. As shown in Fig. S16 in the ESM, the Zn||PDDA@MWCNT-M device delivers the highest energy density of 268 $Wh \cdot kg^{-1}$, outperforming Zn||PDDA@MWCNT-H (252 $Wh \cdot kg^{-1}$), Zn||PDDA@MWCNT-L (242 $Wh \cdot kg^{-1}$), and Zn||PDDA@GS (229 $Wh \cdot kg^{-1}$). In addition, the excellent rate capability of Zn||PDDA@MWCNT-M indicates its superior power output characteristics compared with other cells. The simultaneous enhancement in both energy density and power capability highlights the advantage of the curvature-optimized PDDA@MWCNT-M cathode, which effectively balances strong polyiodide confinement with fast redox kinetics. Benefiting from this balanced energy density and power density, the Zn||PDDA@MWCNT-M also exhibits remarkable stability at 3.0 $A \cdot g^{-1}$ (Fig. 2(d), Figs. S17 and S18 in the ESM), demonstrating the robustness of the optimal structure in PDDA@MWCNT-M. The assembled cell maintains a capacity of 120.2 mAh·g^{-1} after 82,000 cycles (~320 days), corresponding to an ultralow decay rate of only 0.028% per cycle, outperforming all other counterparts. These results demonstrate that the moderate curvature not only accelerates redox reaction kinetics but also enhances interfacial and structural stability during long-term cycling, enabling highly reversible and durable Zn-I_2 electrochemistry [29, 43]. A quantitative comparison between the electrochemical performance summarized in Fig. 2(e) and the structural and thermodynamic

parameters listed in Table S1 in the ESM reveal a clear curvature-performance correlation. The PDDA@MWCNT-M cathode exhibits the most negative adsorption Gibbs free energy together with the highest capacity and energy density, whereas both higher curvature (MWCNT-H) and lower curvature (MWCNT-L or planar GS) display relatively weaker adsorption thermodynamics and inferior electrochemical performance. This result indicates a non-monotonic curvature effect, the moderate curvature optimizes PDDA chain conformation and maximizes the accessibility of quaternary ammonium sites for polyiodide adsorption. As summarized in Fig. 2(f) and Table S2 in the ESM, the Zn||PDDA@MWCNT-M surpasses most previously reported Zn-I_2 systems in both capacity and lifespan, which can be attributed to the curvature-optimized PDDA conformation that strengthens electrostatic anchoring while ensure fast ion diffusion.

To gain molecular level insights into how geometric curvature modulates polyiodide binding and redox behavior, density functional theory (DFT) calculations have been performed on PDDA chains with distinct conformations. Due to the high molecular weight and structural complexity of MWCNT, directly modeling of the interface of full PDDA@MWCNT composite becomes computationally intractable. Therefore, the composite system has been simplified to PDDA chain fragments on curved or flat substrates, validated by the following facts. Firstly, the suppression of the polyiodide species shuttle is dominated by electrostatic interactions between cationic PDDA and anionic polyiodide species [33, 34], while the intrinsic negative charge of carbon substrates have a repulsive effect on polyiodide species and the hollow MWCNT interior shows negligible affinity toward polyiodide species [44–46]. Secondly, long PDDA chains strongly adhere to the surfaces of MWCNT or GS through electrostatic and van der Waals interactions, thereby making the substrates' surface exhibit the essential properties of PDDA [35]. Thirdly, iodine molecules can be physically confined within MWCNT interiors, their extremely low solubility in aqueous media makes them have a negligible contribution to the shuttle effect of iodine [47, 48]. Based on these validated assumptions, the adsorption energies of I_3^- on PDDA chains with different curvatures have been calculated. As illustrated in Fig. 3(a), the adsorption energy exhibits a non-monotonic curvature dependence, where the moderately curved PDDA configuration (PDDA@MWCNT-M) forming the most stable PDDA-I_3^- complex. This trend identifies an optimal geometric conformation for anchoring polyiodides. Subsequently, Fig. 3(b) further evaluated the adsorption behaviors of linear and moderately curved PDDA toward I^-, I_3^-, and I_2. The moderately curved PDDA consistently shows stronger adsorption for all iodine species, revealing that it can effectively suppress polyiodide dissolution and mitigate shuttle effects [4, 35, 49]. To elucidate the origin of this enhancement, the electrostatic potential distributions of flat and curved PDDA chains are analyzed (Figs. 3(c) and 3(d)). In detail, the electrostatic potential of red region is positive, indicating that this region is more likely to obtain electrons, and effectively adsorb the anionic iodine species through the electrostatic attraction effect [9]. The moderately curved PDDA chain shows a more concentrated and intensified positive potential, thereby amplifying Coulombic attraction toward polyiodides. Corresponding Gibbs free energies for the $I^-/I_3^-/I_2$ conversion pathway were also calculated (Fig. 3(e)). The curved PDDA consistently shows lower reaction free energies than the linear configuration, indicating that curvature not only strengthens adsorption thermodynamics but also accelerates interfacial redox kinetics [50, 51]. Collectively, these theoretical calculation findings demonstrate that curvature-induced modulation of PDDA conformation creates a more favorable electrostatic microenvironment for stabilizing iodine intermediates and facilitates reversible redox conversion. This conformation-optimized interaction mechanism fundamentally explains the superior electrochemical performance of PDDA@MWCNT-M in Zn-I_2 batteries.

Based on the above structural and theoretical insights, the subsequent kinetic studies are focused on validating how curvature-optimized PDDA conformations regulate interfacial reaction dynamics. As shown in Fig. S19 in the ESM, the Nyquist plots reveal that Zn||PDDA@MWCNT-M cell exhibits a much smaller semicircle radius than Zn||PDDA@GS, implying lower charge-transfer resistance and enhanced ion diffusion kinetics at

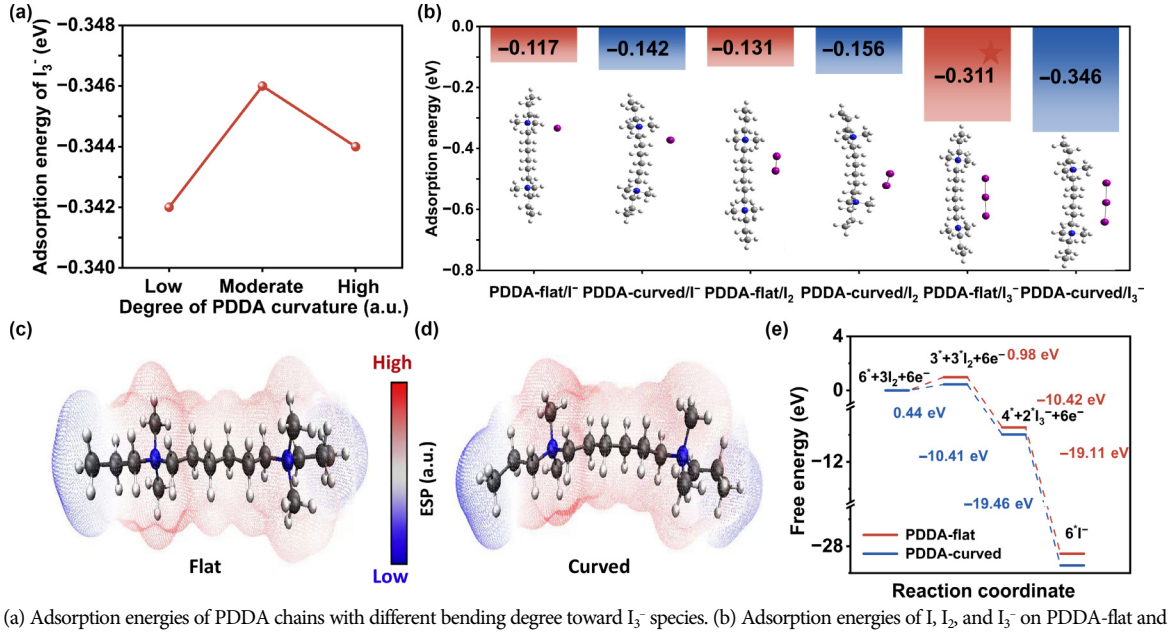

Figure 3 (a) Adsorption energies of PDDA chains with different bending degree toward I_3^- species. (b) Adsorption energies of I, I_2, and I_3^- on PDDA-flat and PDDA-curved chains. Electrostatic potential distributions of (c) flat and (d) curved PDDA chains. (e) Gibbs free energy profiles for the $I/I_3^-/I_2$ redox conversion on PDDA with flat and curved configurations.

the cathode and electrolyte interface [52]. Cyclic voltammetry (CV) further confirms these advantages (Figs. 4(a) and 4(b)). Both electrodes show two characteristic redox couples, the first redox couple (Peaks 1 and 3) correspond to the reversible conversion between iodide and triiodide ions: $3I^- - 2e^- \leftrightarrow I_3^-$, while the second redox couple (Peaks 2 and 4) is attributed to the subsequent conversion between triiodide and molecular iodine: $2I_3^- - 2e^- \leftrightarrow 3I_2$ [35, 53]. At 0.1 mV·s^{-1}, Zn||PDDA@MWCNT-M shows narrow potential gaps (ΔP) of only 65 and 77 mV for the two redox couples, reflecting highly reversible kinetics [49], whereas Zn||PDDA@GS exhibits larger ΔP values of 102 and 131 mV, suggesting more sluggish reaction kinetics. Even at 1.0 mV·s^{-1}, the ΔP values for PDDA@MWCNT-M (169 and 161 mV) remain significantly smaller than those for PDDA@GS (242 and 215 mV), confirming that curvature-enabled PDDA conformations effectively suppress polarization and promote rapid $I^-/I_3^-/I_2$ conversion.

To further elucidate the charge storage mechanism, the peak current (i) and scan rate (v) relationship has been analyzed according to Eqs. (S3) and (S4) in the ESM. The b values for Zn||PDDA@MWCNT-M (0.848/0.837 for Peaks 1/3 and 0.846/0.845 for Peaks 2/4) are higher than Zn||PDDA@GS (0.727/0.641 and 0.833/0.834), indicating that the curved surface electrode favors a mixed diffusion-capacitive process with accelerated interfacial kinetics (Figs. 4(c) and 4(d)) [54]. Moreover, the pseudo-capacitive contribution ratio can be determined based on the Eqs. (S5) and (S6) in the ESM. In detail, the Zn||PDDA@MWCNT-M exhibits capacitive contribution ratios of 71%, 78%, 82%, 86%, and 89% at scan rates of 0.1, 0.3, 0.5, 0.8, and 1.0 mV·s^{-1} respectively, consistently higher than those of Zn||PDDA@GS (56%, 62%, 67%, 75%, and 80%) (Figs. 4(e) and 4(f)). These results collectively confirm that curvature-induced PDDA conformations not only facilitate ion diffusion but also accelerate interfacial charge transfer, resulting in superior pseudocapacitive behavior and redox reversibility.

The self-discharge evaluations further highlight the suppression of side reactions, particularly the polyiodide shuttle effect (Figs. 4(g)–4(i)). After 100 h of rest, Zn||PDDA@MWCNT-M retains 86.4% of its capacity and a high open-circuit voltage of 1.272 V, whereas Zn||PDDA@GS decays rapidly to 46.8% (1.243 V), confirming the superior confinement of polyiodides within the curved interfacial region [39, 55]. In parallel, galvanostatic intermittent titration technique (GITT) measurements also validate this conclusion (Figs. S20 and S21 in the ESM). The calculated diffusion coefficients of Zn||PDDA@MWCNT-M (10^{-8}–10^{-7} cm^2·s^{-1}) are higher than those of PDDA@GS (10^{-9}–10^{-7} cm^2·s^{-1}), confirming that curvature-induced structural advantages facilitate faster Zn^{2+} and I^- transport across the electrode/electrolyte interface [56].

To further track the behavior of polyiodide species during

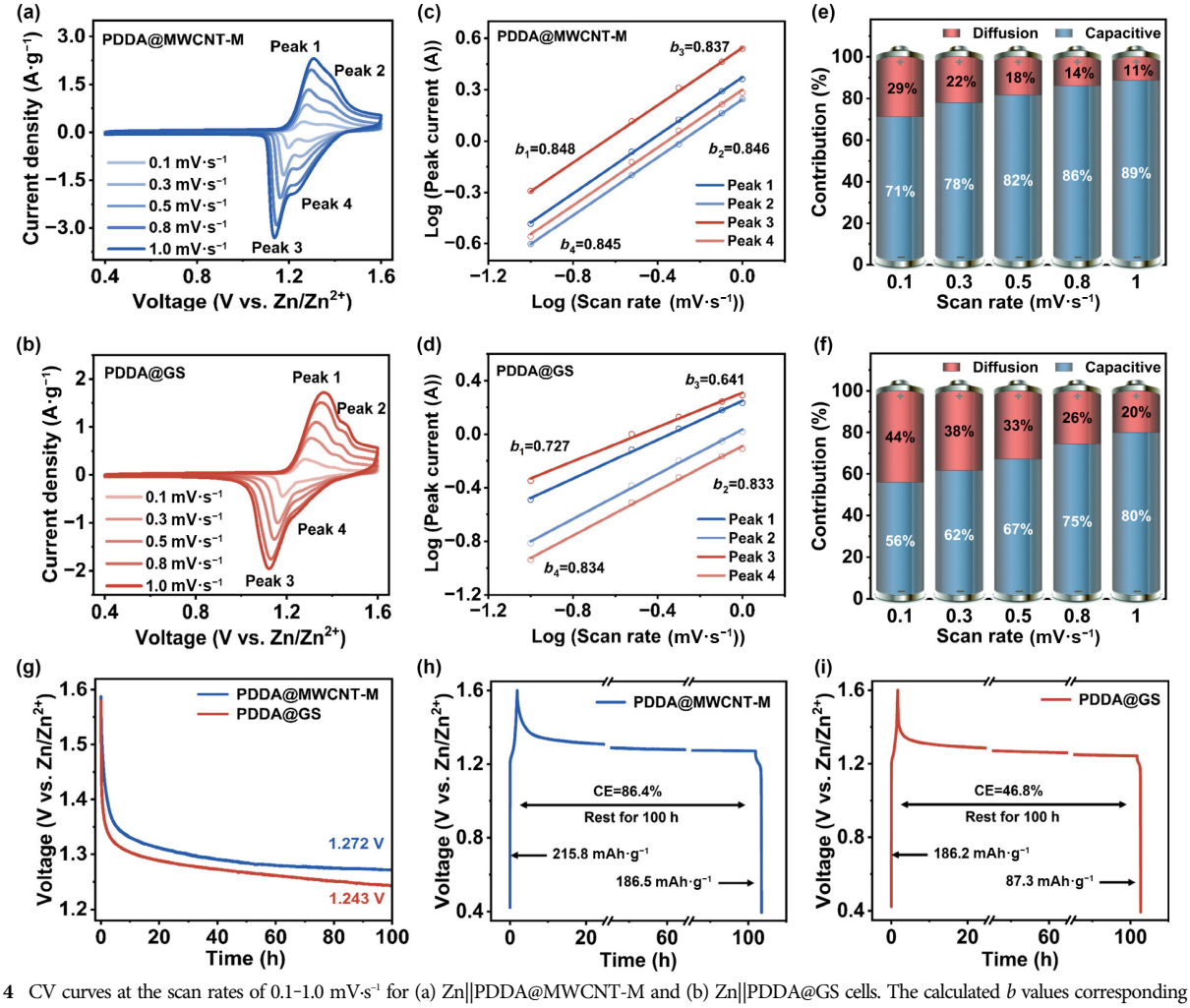

Figure 4 CV curves at the scan rates of 0.1–1.0 mV·s^{-1} for (a) Zn||PDDA@MWCNT-M and (b) Zn||PDDA@GS cells. The calculated b values corresponding to the redox peaks in (c) Zn||PDDA@MWCNT-M and (d) Zn||PDDA@GS cells. The calculated capacitive contribution ratios of (e) Zn||PDDA@MWCNT-M and (f) Zn||PDDA@GS at scan rate of 0.1–1.0 mV·s^{-1}. (g–i) Comparison of the prevent self-discharge capability of Zn||PDDA@MWCNT-M and Zn||PDDA@GS cells.

cycling, *in-situ* UV-Vis spectrophotometry has been performed (Figs. 5(a), 5(b), and Figs. S22-S25 in the ESM). The PDDA@GS cathode exhibits pronounced absorption peaks at 290 and 350 nm, corresponding to the continuous dissolution of I_3^- into the electrolyte [33, 57]. However, the PDDA@MWCNT-M cathode maintains weak and low I_3^- signals throughout the cycling process, demonstrating the effectively confinement of polyiodides within the curved interfacial region. The conversion processes of iodine species in cathodes of Zn||PDDA@MWCNT-M and Zn||PDDA@GS are further analyzed by *ex-situ* X -ray photoelectron spectroscopy (XPS) when the cell has been charged or discharged to different states (Figs. 5(c) and 5(d)). In the initial resting process, both cathodes exhibit the characteristic doublet peaks attributable to I^- species. Upon charging to 1.3 V, both cathodes exhibit the oxidation reaction of I^- to I_3^- and subsequently to I_2, which is consistent with the CV observations [35, 54, 58]. However, upon further charging to 1.6 V, the I_3^- signal completely vanished in PDDA@MWCNT-M electrode, leaving only the doublet peaks for I_2, confirming that all I_3^- had been fully oxidized and without residual intermediates. In contrast, detectable I_3^- even at the end of charge is still found in the PDDA@GS cathode, implying incomplete oxidation conversion and potential shuttle migration in the planar electrode. During discharge to 0.4 V, only I^- specie is detected in PDDA@MWCNT-M, whereas both I_3^- and I^- peaks are still remain for PDDA@GS electrode. To provide more direct real-time evidence for the iodine conversion process and polyiodide confinement, *in-situ* Raman spectroscopy has been further conducted during the charge-discharge process (Fig. S26 in the ESM). For the Zn||PDDA@MWCNT-M cell, characteristic Raman bands corresponding to I_3^- (~110 cm^{-1}) and I_5^- (~160 cm^{-1}) species emerge during the charging process and gradually disappear upon further charging, indicating the progressive oxidation of polyiodides to I_2 [59, 60]. During the subsequent discharge process, these polyiodide signals reappear and finally vanish again at the end of discharge, demonstrating a highly reversible iodine redox process. This reversible evolution suggests that the PDDA@MWCNT-M cathode effectively confines polyiodide intermediates and promotes their rapid redox conversion. In contrast, Zn||PDDA@GS exhibits persistent Raman signals of polyiodide species after a period of charging, indicating that the adsorption capacity of the PDDA@GS is insufficient,

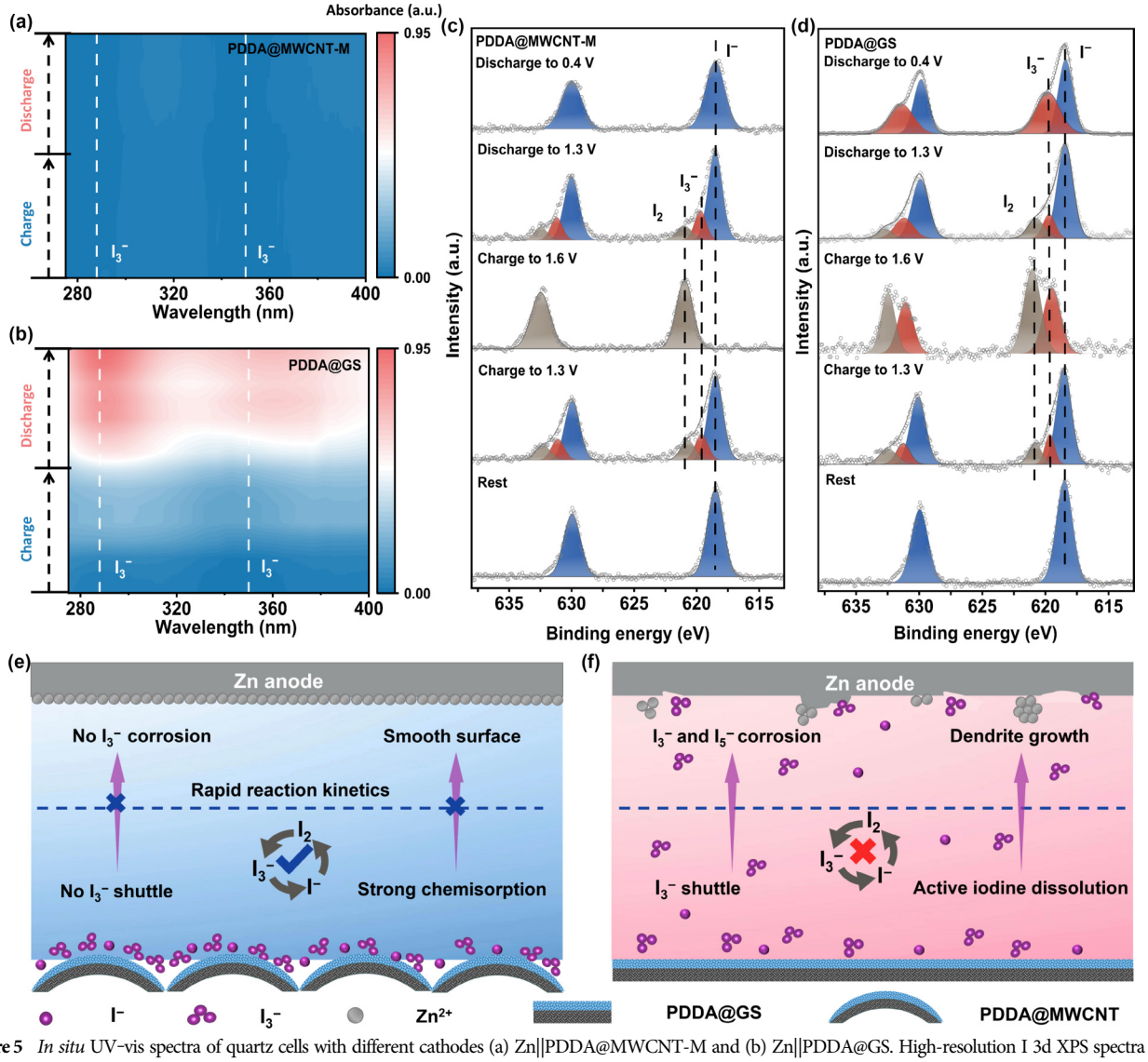

Figure 5 *In situ* UV-vis spectra of quartz cells with different cathodes (a) Zn||PDDA@MWCNT-M and (b) Zn||PDDA@GS. High-resolution I 3d XPS spectra with different cathodes at different states (c) Zn||PDDA@MWCNT-M and (d) Zn||PDDA@GS. Schematic illustration of the reaction mechanism with different cathodes and Zn anode of AZIBs (e) Zn||PDDA@MWCNT-M and (f) Zn||PDDA@GS.

leading to significant polyiodide shuttling. Notably, the iodine conversion pathways observed via *in-situ* Raman spectroscopy are in excellent agreement with *ex-situ* XPS analysis, further confirming that the curvature-optimized PDDA@MWCNT-M cathode effectively suppressed the migration of polyiodide species and enabled highly reversible iodine redox chemistry. The morphology and crystallographic evolution of Zn anodes after prolonged cycling further validate this suppression effect (Figs. S27–S29 in the ESM). The Zn anode paired with Zn||PDDA@MWCNT-M cell remains smooth and dense, whereas the counterpart in Zn||PDDA@GS suffers severe dendritic corrosion and by-product accumulation, verifying that the curved cathode effectively restrains polyiodide shuttling and mitigates Zn corrosion during repeated stripping/plating.

Finally, to provide a visual summary of above findings, a schematic of the charge/discharge processes in Zn-I_2 cells with different cathode configurations is presented (Figs. 5(e) and 5(f)). For the planar PDDA@GS configuration, the limited electrostatic binding and flat interfacial geometry fail to effectively stabilize polyiodide species, leading to pronounced shuttle migration and sluggish $I^-/I_3^-/I_2$ redox conversion. In contrast, PDDA@MWCNT-M integrates the intrinsic tubular curvature of MWCNT with a conformal PDDA coating, forming a confined nanoscale electrostatic environment that amplifies local electric fields, strengthens polyiodide anchoring, and accelerates reversible $I^-/I_3^-/I_2$ redox reactions. Specifically, the moderate curvature of MWCNT-M promotes an extended PDDA geometry that (1) concentrates positive electrostatic potential around quaternary ammonium sites, thereby amplifies Coulombic anchoring of $I^-/I_3^-/I_2$ intermediates; (2) increases the exposure and accessibility of active binding sites while preserving ion transport channels, which lowers charge-transfer resistance and enhances pseudocapacitive contribution; and (3) stabilizes the interfacial microstructure under prolonged cycling and high loading, effectively suppressing polyiodide shuttling and mitigating Zn anode corrosion. Collectively, the curvature-electrostatics coupling provides a unified explanation for the superior iodine adsorption, accelerated and reversible $I^-/I_3^-/I_2$ conversion, and ultrastable electrochemical performance observed for the PDDA@MWCNT-M electrode.

Encouraged by these mechanistic and kinetic advantages, we have further evaluated the practical applicability of the PDDA@MWCNT-M cathode under realistic conditions. At a high areal iodine loading of 7.1 mg·cm^{-2}, the Zn-I_2 coin cell delivering a high CE of 98.24% at 0.1 A·g^{-1}, underscoring the strong immobilization of polyiodide species (Fig. 6(a)). Even under a high current density of 2.0 A·g^{-1}, the cell retains 87.8% of its initial capacity after over 10,000 cycles, confirming its exceptional long-term durability (Fig. 6(b)). Moreover, pouch-type Zn-I_2 batteries (3.0 cm × 3.0 cm) have been assembled using the PDDA@MWCNT-M cathode to evaluate large-format adaptability (Fig. 6(c)). As presented in Fig. 6(d), the pouch cell delivers a high discharge capacity of 190.2 mAh·g^{-1} after 300 cycles at 0.1 A·g^{-1}, corresponding to 93.9% capacity retention. Based on the mass of active materials, the device achieves a gravimetric energy density of 251 Wh·kg^{-1}, highlighting the strong potential of this cathode design for practical aqueous Zn-I_2 batteries (Fig. S30

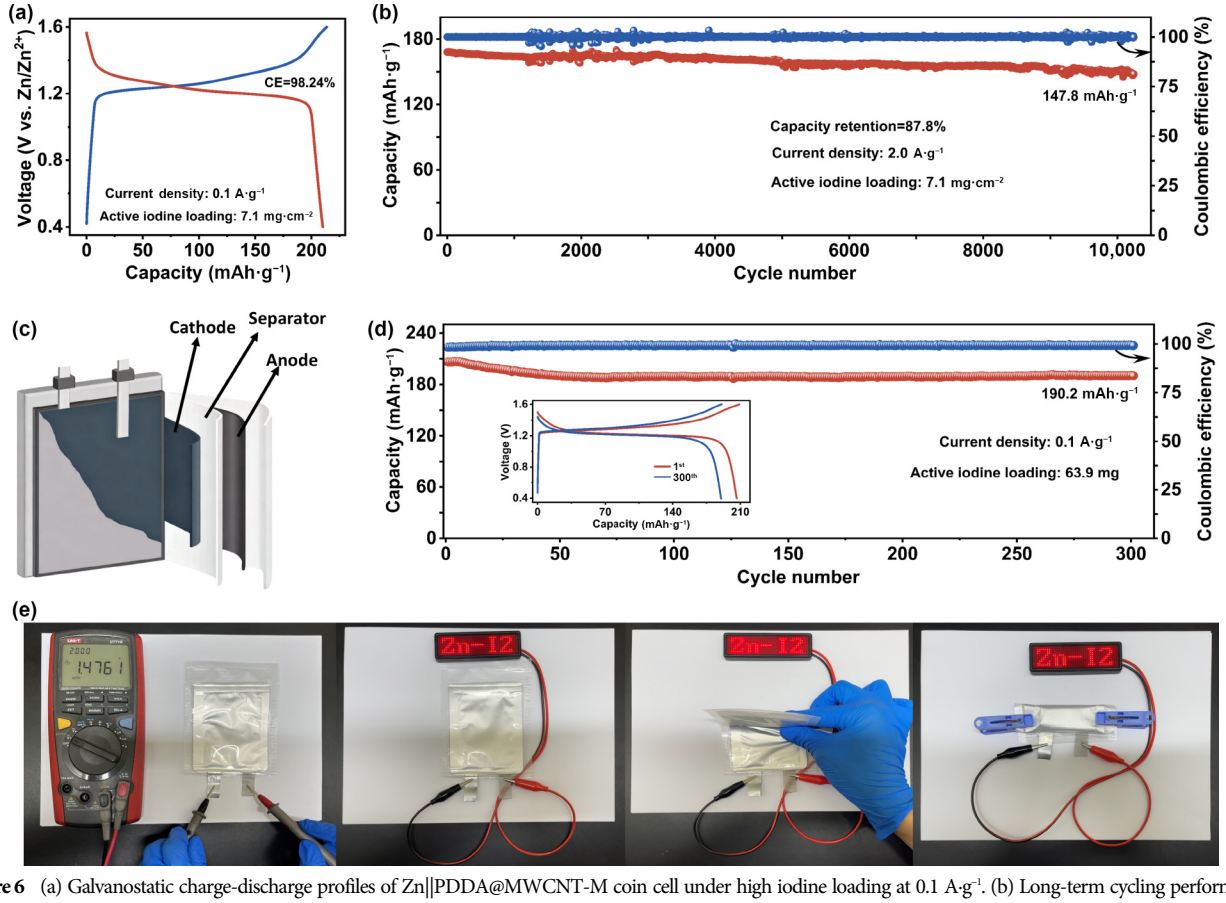

Figure 6 (a) Galvanostatic charge-discharge profiles of Zn||PDDA@MWCNT-M coin cell under high iodine loading at 0.1 A·g^{-1}. (b) Long-term cycling performance of the Zn||PDDA@MWCNT-M at 2.0 A·g^{-1}. (c) Schematic diagram of Zn-I_2 pouch batteries. (d) Cycling stability of the pouch cell at 0.1 A·g^{-1} (3.0 cm × 3.0 cm). (e) Demonstration of pouch-cell flexibility and mechanical robustness: powering an LED panel spelling "Zn-I_2" under flat and bent (90°) states.

in the ESM). Encouragingly, a single pouch cell provides a stable working voltage of ~1.48 V, which can directly power an LED panel spelling out "Zn-I_2". Even under 90° bending or repeated mechanical deformation, the LED panel remains steadily illuminated, demonstrating outstanding mechanical robustness and operational safety (Fig. 6(e)). From a practical perspective, the PDDA@MWCNT-M cathode is fabricated through a simple solution-based assembly by using commercially available MWCNT and PDDA, avoiding complex synthesis routes and high-temperature treatments. This mild and scalable process is compatible with conventional slurry coating and roll-to-roll electrode manufacturing, providing a feasible pathway for large-scale production. In addition, the key components used in this work including Zn foil, iodine, carbon hosts, and PDDA are inexpensive and commercially available, enabling a relatively low material cost compared with many previously reported carbon-based cathodes (Table S3 in the ESM). Collectively, the combination of high energy density, long cycling durability, mechanical robustness, and scalable low-cost fabrication highlights the practical potential of the PDDA@MWCNT-M cathode. Therefore, the established molecular curvature engineering can be developed as a promising strategy for developing high-performance aqueous Zn-I_2 energy-storage systems.

3 Conclusions

In summary, this work elucidates how nanoscale curvature modulates cationic polymer configurations and thereby enhances polyiodide immobilization in aqueous Zn-I_2 batteries. By assembling PDDA on carbon hosts with distinct geometric curvatures, we reveal that a moderately curved MWCNT facilitates a more ordered and electrostatically active cationic microenvironment compared to planar GS or excessively/insufficiently curved MWCNT. This curvature-optimized interfacial structure effectively suppresses polyiodide shuttling, accelerates $I^-/I_3^-/I_2$ redox kinetics, and achieves exceptional long-term cycling stability (82,000 cycles at 3.0 $A{\cdot}g^{-1}$ and 3,569 cycles at 0.1 $A{\cdot}g^{-1}$ over nearly one year). DFT calculations further confirm that curvature-regulated PDDA chains strengthen polyiodide adsorption and reduce the Gibbs free energy barriers for $I^-/I_3^-/I_2$ conversion. These insights establish a clear curvature-function relationship for cationic interfacial layers, addressing a long-standing challenge in Zn-I_2 batteries and paving the way for advanced energy storage designs.

Acknowledgements

The work was financially supported by the National Natural Science Foundation of China (U21A20172, U21A6004, 52402284, 52403041), Fundamental Research Program of Shanxi Province (202203021221007, 202403021222021), Excellent Graduate Mentor Team Project in Shanxi Province (2025TD03) and the Open Fund of the Key Lab of Organic Optoelectronics & Molecular Engineering. And the authors sincerely thank Professor Hu Tuoping's research group in the School of Chemistry and Chemical Engineering at North University of China for conducting the *in-situ* Raman spectroscopy tests.

Declaration of conflicting interests

The authors declare no conflicting interests regarding the content of this article.

Data availability

All data needed to support the conclusions in the paper are presented in the manuscript and/or the Supplementary Materials. Additional data related to this paper may be requested from the corresponding author upon request.

Electronic Supplementary Material Supplementary material (including materials synthesis and preparation, assembly of the Zn–I_2 battery, structural and morphological characterizations (TEM, SEM, and XRD), UV–vis spectroscopy, electrochemical measurements, capacity contribution calculation formulas, and a comparative table summarizing the performance of advanced Zn–I_2 batteries) is available in the online version of this article at https://doi.org/10.26599/NRE.2026.9120227.

References

[1] Xie, C. X.; Wang, C.; Xu, Y.; Li, T. Y.; Fu, Q.; Li, X. F. Reversible multielectron transfer I^-/IO_3^- cathode enabled by a hetero-halogen electrolyte for high-energy-density aqueous batteries. *Nat. Energy* **2024**, *9*, 714–724.

[2] Wang, F. F.; Ma, R. L.; Chen, Z. H.; Yin, T. Y.; Yan, Z. J.; Chi, S. J.; Jiao, M. G.; Yang, C. P.; Yang, Q. H. Click chemistry-inspired fixation catalysis for long-life zinc-iodine batteries. *Adv. Mater.* **2026**, *38*, e11980.

[3] Dong, Y.; Hu, H. L.; Liang, P.; Xue, L. L.; Chai, X. L.; Liu, F. M.; Yu, M.; Cheng, F. Y. Dissolution, solvation and diffusion in low-temperature zinc electrolyte design. *Nat. Rev. Chem.* **2025**, *9*, 102–117.

[4] He, X. F.; Kong, X. Y.; Wen, L. P. A promising solution for highly reversible zinc metal anode chemistry: Functional gradient interphase. *Nano Res. Energy* **2024**, *3*, e9120100.

[5] Liang, G. J.; Liang, B. C.; Chen, A.; Zhu, J. X.; Li, Q.; Huang, Z. D.; Li, X. L.; Wang, Y.; Wang, X. Q.; Xiong, B. et al. Development of rechargeable high-energy hybrid zinc-iodine aqueous batteries exploiting reversible chlorine-based redox reaction. *Nat. Commun.* **2023**, *14*, 1856.

[6] Sun, Y.; Li, S. Q.; Li, G. P.; Su, Y.; Sun, M. F.; Wang, X. L.; Wang, J. X.; Yu, W. S.; Dong, X. T.; Liu, D. T. Iodine-confined porous covalent triazine frameworks enable ultra-stable aqueous zinc-iodine batteries. *Chem. Eng. J.* **2025**, *524*, 169752.

[7] Yang, X.; Xie, M. H.; Yan, Z. J.; Ruan, H.; Yang, C. P.; Guo, Z. P.; Zheng, Z. J. High-iodine-loading quasi-solid-state zinc-iodine batteries enabled by a continuous ion-transport network. *Energy Environ. Sci.* **2025**, *18*, 4730–4739.

[8] Liu, C.; Li, Q.; Lin, Y. L.; Wei, Z. Q.; Yang, Y. H.; Han, C. P.; Zhu, M. S.; Zhang, H. Y.; Li, H. F. Functional group differentiation of isomeric solvents enables distinct zinc anode chemistry. *Nano Res. Energy* **2023**, *2*, e9120064.

[9] Zhang, L. Q.; Huang, J. J.; Guo, H. L.; Ge, L. F.; Tian, Z. H.; Zhang, M. J.; Wang, J. T.; He, G. J.; Liu, T. X.; Hofkens, J. et al. Tuning ion transport at the anode-electrolyte interface via a sulfonate-rich ion-exchange layer for durable zinc-iodine batteries. *Adv. Energy Mater.* **2023**, *13*, 2203790.

[10] Tan, L. C.; Wei, J.; Xue, L. J.; Luo, D.; Chen, G. Y.; Chu, Y.; Wang, J. Y.; Zong, K.; Song, X. M.; Yang, L. et al. Regulating the electron structure of covalent organic frameworks to enable excellent cycle life and high rate toward advanced Zn−I_2 batteries. *Adv. Funct. Mater.* **2025**, *35*, 2416931.

[11] Chen, G. H.; Kang, Y. H.; Yang, H. Y.; Zhang, M. H.; Yang, J.; Lv, Z. H.; Wu, Q. L.; Lin, P. X.; Yang, Y.; Zhao, J. B. Toward forty thousand-cycle aqueous zinc-iodine battery: Simultaneously inhibiting polyiodides shuttle and stabilizing zinc anode through a suspension electrolyte. *Adv. Funct. Mater.* **2023**, *33*, 2300656.

[12] Lu, K.; Hu, Z. Y.; Ma, J. Z.; Ma, H. Y.; Dai, L. M.; Zhang, J. T. A

rechargeable iodine-carbon battery that exploits ion intercalation and iodine redox chemistry. *Nat. Commun.* **2017**, *8*, 527.

[13] Lee, J.; Srimuk, P.; Fleischmann, S.; Ridder, A.; Zeiger, M.; Presser, V. Nanoconfinement of redox reactions enables rapid zinc iodide energy storage with high efficiency. *J. Mater. Chem. A* **2017**, *5*, 12520–12527.

[14] Yang, H. J.; Qiao, Y.; Chang, Z.; Deng, H.; He, P.; Zhou, H. S. A metal-organic framework as a multifunctional ionic sieve membrane for long-life aqueous zinc-iodide batteries. *Adv. Mater.* **2020**, *32*, 2004240.

[15] Chen, Q. R.; Hao, J. N.; Zhu, Y. L.; Zhang, S. J.; Zuo, P. P.; Zhao, X.; Jaroniec, M.; Qiao, S. Z. Anti-swelling microporous membrane for high-capacity and long-life Zn–I_2 batteries. *Angew. Chem., Int. Ed.* **2025**, *64*, e202413703.

[16] Yang, Y. Q.; Liang, S. Q.; Lu, B. A.; Zhou, J. Eutectic electrolyte based on *N*-methylacetamide for highly reversible zinc-iodine battery. *Energy Environ. Sci.* **2022**, *15*, 1192–1200.

[17] Zhang, S. J.; Hao, J. N.; Wu, H.; Chen, Q. R.; Ye, C.; Qiao, S. Z. Protein interfacial gelation toward shuttle-free and dendrite-free Zn-iodine batteries. *Adv. Mater.* **2024**, *36*, 2404011.

[18] Hu, Z. Y.; Wang, X. W.; Du, W. C.; Zhang, Z. C.; Tang, Y. C.; Ye, M. H.; Zhang, Y. F.; Liu, X. Q.; Wen, Z. P.; Li, C. C. Crowding effect-induced zinc-enriched/water-lean polymer interfacial layer toward practical Zn-iodine batteries. *ACS Nano* **2023**, *17*, 23207–23219.

[19] Tian, Y. D.; Chen, S.; He, Y. L.; Chen, Q. W.; Zhang, L. L.; Zhang, J. T. A highly reversible dendrite-free Zn anode via spontaneous galvanic replacement reaction for advanced zinc-iodine batteries. *Nano Res. Energy* **2022**, *1*, 9120025.

[20] Zhu, L. F.; Guan, X. W.; Li, P.; Ma, Y. B.; Zhang, Z. F.; Yuan, Z. L.; Zhang, C. C.; Wang, Y.; Li, H.; Jia, B. H. et al. Waste coffee grounds-derived micropores carbon framework as an efficient iodine host for zinc iodine battery. *Energy Environ. Mater.* **2025**, *8*, e70045.

[21] Liu, S. Y.; Zhang, J. D.; Gao, Y. M.; Liu, B. Q.; Luo, Y. Q.; Fang, K. X.; Dong, M. L.; Zhang, Q.; Jin, Z. S. Iodine species anchored and converted by CoO/Co heterostructure in confined micro-mesoporous carbon nanoreactors for high-performance zinc-iodine batteries. *Chem. Eng. J.* **2025**, *526*, 171429.

[22] Liu, H. T.; Liu, F.; Qu, Z. H.; Chen, J. L.; Liu, H.; Tan, Y. Q.; Guo, J. B.; Yan, Y.; Zhao, S.; Zhao, X. S. et al. High sulfur loading and shuttle inhibition of advanced sulfur cathode enabled by graphene network skin and N, P, F-doped mesoporous carbon interfaces for ultra-stable lithium sulfur battery. *Nano Res. Energy* **2023**, *2*, e9120049.

[23] He, Z. K.; Jiao, Y. Y.; Jin, X. Y.; Yu, X.; Kang, H. W. Construction of mesoporous cationic framework polymer for high performance zinc-iodine batteries. *Electrochim. Acta* **2025**, *543*, 147539.

[24] Guo, S. D.; Hu, S. L.; Li, S. L.; Wang, D.; Zhang, S. Q.; Luo, L. W.; Hong, G.; Yao, Y. G.; Han, C. P. Cathode design via iron-coordinated covalent organic frameworks facilitating four-electron transfer to achieve high-capacity aqueous zinc-iodine batteries. *ACS Nano* **2025**, *19*, 32533–32545.

[25] Han, Z. Y.; Fan, X. K.; Zhang, L. X.; Wang, K.; Wang, J.; Li, H.; Jiang, G. M.; Li, W. H.; Wang, L. P.; Ma, Y. Z. et al. Regular mesoporous nanosheets with mesoscopic high surface pore curvature and accelerated ion-transport channels. *Matter* **2025**, *8*, 102164.

[26] Luo, Y. T.; Bai, Y.; Mistry, A.; Zhang, Y. W.; Zhao, D. X.; Sarkar, S.; Handy, J. V.; Rezaei, S.; Chuang, A. C.; Carrillo, L. et al. Effect of crystallite geometries on electrochemical performance of porous intercalation electrodes by multiscale operando investigation. *Nat. Mater.* **2022**, *21*, 217–227.

[27] Jiang, D.; Xu, R. B.; Bai, L.; Hill, J. P.; Henzie, J.; Zhu, L. Y.; Xia, W.; Bu, R.; Zhao, Y. J.; Kang, Y. Q. et al. Substrate curvature-induced regulation of charge distribution of covalent organic frameworks promotes capacitive deionization. *Adv. Funct. Mater.* **2024**, *34*, 2407479.

[28] Wang, B. Q.; Wang, M.; Fan, Z. T.; Ma, C.; Xi, S. B.; Chang, L. Y.; Zhang, M. S.; Ling, N.; Mi, Z. Y.; Chen, S. H. et al. Nanocurvature-induced field effects enable control over the activity of single-atom electrocatalysts. *Nat. Commun.* **2024**, *15*, 1719.

[29] Sun, Y. C.; Lv, X. Z.; Li, X.; Sun, Z. Y.; Li, R. H.; Cao, Y. Y.; Huang, J. H.; Wang, H. Y. Curvature and heterojunction customized iodine chemistry for high-capacity and stable zinc-iodine/manganese hybrid batteries. *Chem. Eng. J.* **2026**, *529*, 172948.

[30] Su, J. J.; Musgrave III, C. B.; Song, Y.; Huang, L. B.; Liu, Y.; Li, G.; Xin, Y. E.; Xiong, P.; Li, M. M. J.; Wu, H. R. et al. Strain enhances the activity of molecular electrocatalysts via carbon nanotube supports. *Nat. Catal.* **2023**, *6*, 818–828.

[31] Munz, M.; Poon, J.; Frandsen, W.; Cuenya, B. R.; Kley, C. S. Nanoscale electron transfer variations at electrocatalyst-electrolyte interfaces resolved by *in situ* conductive atomic force microscopy. *J. Am. Chem. Soc.* **2023**, *145*, 5242–5251.

[32] Jeon, B. J.; Lee, Y. H.; Jeong, K. M. Unveiling the impact of electrode curvature on N/P ratio variations in cylindrical lithium-ion batteries. *Energy Storage Mater.* **2025**, *76*, 104117.

[33] Zhang, G. Y.; Guo, K.; Zhou, L.; Wu, Y. T.; Ma, Z. X.; Chang, Y. Z.; Li, Y. P.; Liu, S. J.; Zhu, S.; Han, G. Y. Cationic polymer-engineered cathode for shuttle-free and ultra-long cyclic aqueous Zn–I_2 batteries. *Chin. Chem. Lett.*, in press, DOI: 10.1016/j.cclet.2025.111870.

[34] Yuan, W. T.; Qu, X. H.; Wang, Y. Y.; Li, X. T.; Ru, X. H.; Jia, D. G.; Zhao, L. D.; Hou, Y. Q.; Shen, J. X.; Shen, Z. X. et al. Polycationic polymer functionalized separator to stabilize aqueous zinc-iodine batteries. *Energy Storage Mater.* **2025**, *76*, 104130.

[35] Zhou, L.; Zhang, G. Y.; Guo, J. Z.; Liu, S. J.; Chang, Y. Z.; Zhang, Y.; Li, Y. P.; Zhu, S.; Han, G. Y. Electrostatic-immobilized polyiodides via bifunctional quaternary ammonium binder for shuttle-free and ultra-stable Zn–I_2 batteries. *Adv. Funct. Mater.* **2026**, *36*, e13527.

[36] Chen, L. T.; Huang, S.; Feng, Z. F.; Lin, Z. X.; Huang, H. L.; Ye, M. H.; Zhang, Y. F.; Wen, Z. P.; Tang, Y. C.; Liu, X. Q. et al. Local electric field microenvironment-induced dynamic spatial confinement to stabilize I^+ toward high-mass-loading and stable zinc-iodine batteries. *Angew. Chem., Int. Ed.* **2025**, *64*, e202510737.

[37] Wu, H.; Zhang, S. J.; Vongsvivut, J.; Jiang, Y. L.; Hao, J. N.; Qiao, S. Z. Quasi-solid cathode additive enables highly reversible four-electron $I^-/I^0/I^+$ conversion in aqueous Zn–I_2 batteries. *Adv. Mater.* **2026**, *38*, e11680.

[38] Jeon, Y.; Sung, J.; Kim, D.; Seo, C.; Cheong, H.; Ouchi, Y.; Ozawa, R.; Hamaguchi, H. O. Structural change of 1-butyl-3-methylimidazolium tetrafluoroborate + water mixtures studied by infrared vibrational spectroscopy. *J. Phys. Chem. B* **2008**, *112*, 923–928.

[39] Wu, H.; Zhang, S. J.; Vongsvivut, J.; Jaroniec, M.; Hao, J. N.; Qiao, S. Z. Aqueous zinc-iodine batteries with ultra-high loading and advanced performance. *Joule* **2025**, *9*, 102000.

[40] Feng, G. L.; Yang, X.; Liu, X. H.; Wang, Y. B.; Xie, Y. T.; Dong, P. P.; Jiao, X. X.; Xu, C. L.; Zhao, J. M.; Hu, Y. S. et al. Microbially glycolysis-regulated hard carbons for sodium-ion batteries. *Nano Energy* **2025**, *136*, 110728.

[41] Liu, Y. Y.; Shi, H. D.; Yang, M. Z.; Wang, H. D.; Ma, Y. X.; Li, X. F.; Jin, D. K.; Ma, C. D.; Ren, Z. H.; Shi, X. Y. et al. Kilogram-scale production of ultrafast-charging micro-expanded graphite anode toward high-power and long-life Ah-level pouch batteries. *Adv. Mater.* **2025**, *37*, e06584.

[42] Kim, T. H.; Jeon, E. K.; Ko, Y.; Jang, B. Y.; Kim, B. S.; Song, H. K. Enlarging the *d*-spacing of graphite and polarizing its surface charge for driving lithium ions fast. *J. Mater. Chem. A* **2014**, *2*, 7600–7605.

[43] Yan, W. B.; Liu, Y.; Qiu, J. Z.; Tan, F. P.; Liang, J. H.; Cai, X. Z.; Dai, C. L.; Zhao, J. Q.; Lin, Z. F. A tripartite synergistic optimization strategy for zinc-iodine batteries. *Nat. Commun.* **2024**, *15*, 9702.

[44] Jin, X. T.; Song, L.; Dai, C. L.; Xiao, Y. K.; Han, Y. Y.; Li, X. Y.; Wang, Y.; Zhang, J. T.; Zhao, Y.; Zhang, Z. P. et al. A flexible

aqueous zinc-iodine microbattery with unprecedented energy density. *Adv. Mater.* **2022**, *34*, 2109450.
[45] Yin, D. D.; Li, B. Y.; Zhao, L. Y.; Gao, N.; Zhang, Y. N.; Feng, J.; Cui, X. F.; Xiao, C. H.; Su, Y. Q.; Xi, K. et al. Polymeric iodine transport layer enabled high areal capacity dual plating zinc-iodine battery. *Angew. Chem., Int. Ed.* **2025**, *64*, e202418069.
[46] Li, S. B.; Nie, Y. H.; Wang, Y. A.; Feng, G.; Li, Q. Y.; Ma, Q. Y.; Zhao, C. J.; Xie, Y. H.; Jin, M. L.; Luo, D. et al. Quantum size effect synergizes space-limited domain action for advanced aqueous zinc-iodine batteries. *Adv. Mater.* **2026**, *38*, e14577.
[47] Wu, S. C.; Lin, S. M.; Lo, H. A.; Tang, S. Y.; Hsu, Y. C.; Peng, Y. R.; Gu, B. N.; Chen, Y. T.; Shen, Y. C.; Wu, T. S. et al. Design of electrolyte using deep eutectic solvents for high-performance rechargeable nickel-iodine batteries. *Small* **2025**, *21*, 2412549.
[48] Liu, M. Y.; Abdalla, K. K.; Xu, M.; Li, X. Q.; Wang, R. Z.; Li, Q.; Zhang, X. R.; Lv, Y. N.; Wang, Y. Y.; Sun, X. M. et al. "Proton-iodine" regulation of protonated polyaniline catalyst for high-performance electrolytic Zn–I_2 batteries. *Nano-Micro Lett*. **2026**, *18*, 79.
[49] Chen, Z. X.; Zhang, J.; Zhou, C. C.; Guo, S.; Wu, D. X.; Zhao, Z. W.; Wang, Z. T.; Li, J.; Xing, Z. Y.; Rao, P. et al. Sulfonated lignin binder blocks active iodine dissolution and polyiodide shuttle toward durable zinc-iodine batteries. *Adv. Energy Mater.* **2025**, *15*, 2404814.
[50] Yang, J. L.; Liu, H. H.; Zhao, X. X.; Zhang, X. Y.; Zhang, K. Y.; Ma, M. Y.; Gu, Z. Y.; Cao, J. M.; Wu, X. L. Janus binder chemistry for synchronous enhancement of iodine species adsorption and redox kinetics toward sustainable aqueous Zn–I_2 batteries. *J. Am. Chem. Soc.* **2024**, *146*, 6628–6637.
[51] Liu, L.; Zhang, L. H.; Liu, Y. Y.; Zhang, S. L.; Wang, R.; Li, F. J.; Li, H. B.; Hao, J. N.; Zhang, C. F.; Guo, Z. P. Enhanced redox kinetics of aqueous $I^-/I_2/I^+$ conversion chemistry in hydrated eutectic electrolyte over a wide temperature range. *Adv. Energy Mater.* **2025**, *15*, 2501460.
[52] Zhou, L.; Wang, N.; Chang, Y. Z.; Zhu, S.; Zhang, Y.; Hou, W. J.; Zhao, Y.; Han, G. Y. Polypyrrole polymerized by iodine oxidation for zinc-iodine batteries with high stability. *J. Energy Storage* **2024**, *88*, 111538.
[53] Wang, Y. Y.; Jin, X. R.; Xiong, J. W.; Zhu, Q. Y.; Li, Q.; Wang, R. Z.; Li, J. Z.; Fan, Y. C.; Zhao, Y.; Sun, X. M. Ultrastable electrolytic Zn–I_2 batteries based on nanocarbon wrapped by highly efficient single-atom Fe-NC iodine catalysts. *Adv. Mater.* **2024**, *36*, 2404093.
[54] Wang, N.; Ma, Y. Y.; Chang, Y. Z.; Feng, L. P.; Liu, H. C.; Li, B. Q.; Li, W. X.; Liu, Y. Y.; Han, G. Y. Armoring the cathode with starch gel enables shuttle-free zinc-iodine batteries. *J. Colloid Interface Sci.* **2024**, *665*, 491–499.
[55] Wu, H.; Hao, J. N.; Zhang, S. J.; Jiang, Y. L.; Zhu, Y. L.; Liu, J. H.; Davey, K.; Qiao, S. Z. Aqueous zinc-iodine pouch cells with long cycling life and low self-discharge. *J. Am. Chem. Soc.* **2024**, *146*, 16601–16608.
[56] Jia, D. D.; Shen, Z. L.; Tan, H.; Zheng, K.; Tao, M. M.; Li, H. Q.; Lv, Y. H.; Sang, Y. H.; Ma, L. B.; Zhou, W. J. et al. Dual-enhanced iodine confinement and conversion of single-atom Mn–N_3–C catalyst for long-life electrolytic Zn–I_2 batteries. *Adv. Energy Mater.* **2026**, *16*, e05589.
[57] Guo, X. T.; Xu, H. Y.; Qiu, Z. M.; Li, Q.; Li, N. N.; Yang, Z. B.; Li, W. T.; Lian, Y.; Li, Q.; Sui, Y. W. et al. Heteroatom-modulated asymmetric cobalt single-atom catalysts on MOF-derived carbon enabling durable zinc-iodine batteries. *Adv. Mater.* **2025**, *37*, e14035.
[58] Zhang, L. Q.; Luo, K.; Gong, J. M.; Zhou, Y. Z.; Guo, H. L.; Yu, Y.; He, G. J.; Gohy, J. F.; Parkin, I. P.; Hofkens, J. et al. Unlocking durable and sustainable zinc-iodine batteries via molecularly engineered polyiodide reservoirs. *Angew. Chem., Int. Ed.* **2025**, *64*, e202506822.
[59] Yin, T. Y.; Chen, M. X.; Yan, Z. J.; Wang, F. F.; Luo, Z. Y.; Umer, S.; Chen, Z. H.; Yue, N.; Lv, W.; Yang, C. P. Dual-function high-entropy alloy nanocatalysts enable long-life aqueous zinc-iodine batteries. *Adv. Sustainable Syst.* **2025**, *9*, e01175.
[60] Ma, Y. J.; Meng, X. T.; Wang, X. Y.; Du, Y. D.; Qi, J.; Zou, H. Q.; Li, J. C.; Jiang, Z. H.; Qiu, J. S. Local polarity engineering via unsaturated Cu–N_3 sites for enhanced iodine redox chemistry in zinc-iodine batteries. *Angew. Chem., Int. Ed.* **2026**, *65*, e25573.

Lin Zhou is now a PhD candidate at the Institute of Molecular Science, Shanxi University, China. She is working on the synthesis and fabrication of high-performance aqueous zinc-iodine battery materials.

Wenyan Zan received her PhD degree in Chemistry from Lanzhou University in December 2016. During her doctoral studies, she was a joint-training PhD student at the Department of Materials Science and Nano Engineering, Rice University, USA from December 2014 to December 2016. Currently, she is an associate professor and master's supervisor at Shanxi University, China. She has long been engaged in the research of advanced nanomaterials for electrochemical energy conversion, focusing on experimental synthesis and theoretical investigation in areas such as hydrogen evolution reaction, CO_2 electroreduction, and charge transport mechanisms.

Sheng Zhu received his Ph.D. degree from the College of Chemistry and Molecular Engineering at Peking University in 2021. Currently, he is an associate professor at the Institute of Molecular Science, Shanxi University. His research is dedicated to the design, synthesis, and application of carbon-based nanomaterials. He has published over 50 papers as the first or corresponding author in prestigious journals including *National Science Review*, *Accounts of Materials Research*, *Angewandte Chemie International Edition*, *Cell Reports Physical Science*, *Advanced Functional Materials*, *ACS Materials Letters*, and *Energy Storage Materials*. He has led or participated in several national and provincial-level research projects. Additionally, he serves as a committee member of the Shanxi Committee for Advanced Electrochemistry and Energy Storage Technologies.

Gaoyi Han received his Ph.D. degree from the School of Chemistry and Chemical Engineering at Nanjing University. He is currently a professor and doctoral supervisor at Shanxi University. His research focuses on energy storage materials and devices. He has published over 200 papers in renowned academic journals such as *Advanced Materials*, *Angewandte Chemie International Edition*, *Advanced Functional Materials*, and holds more than 10 authorized national invention patents. He has been recognized as a New Century Excellent Talent by the Ministry of Education and received the Shanxi Provincial "May Fourth" Youth Medal. Additionally, he leads the Shanxi "1331 Project" Key Innovation Team for Inorganic Energy Materials, and serves as the Chair of the Electrochemistry and Energy Storage Technology Committee of the Shanxi Chemical Society.